Electron-Energy Loss Study of Nonlocal Effects in Connected Plasmonic Nanoprisms

Aeneas Wiener,[†,‡] Huigao Duan,[§,⊥] Michel Bosman,[§] Andrew P. Horsfield,[‡] John B. Pendry,[†] Joel K. W. Yang,[§,*] Stefan A. Maier,[†] and Antonio I. Fernández-Domínguez[†,*]

[†]Department of Physics, Imperial College London, London SW7 2AZ, United Kingdom, [‡]Department of Materials, Imperial College London, London SW7 2AZ, United Kingdom, [§]Institute of Materials Research and Engineering, A*STAR (Agency for Science, Technology and Research), 3 Research Link, Singapore 117602, Singapore, and [⊥]College of Physics and Microelectronics, Hunan University, Changsha 410082, China

ABSTRACT

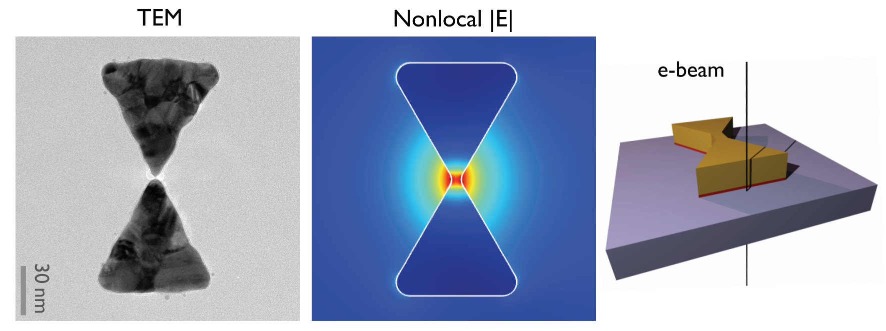

We investigate the emergence of nonlocal effects in plasmonic nanostructures through electron-energy loss spectroscopy. To theoretically describe the spatial dispersion in the metal permittivity, we develop a full three-dimensional nonlocal hydrodynamic solution of Maxwell's equations in frequency domain that implements the electron beam as a line current source. We use our numerical approach to perform an exhaustive analysis of the impact of nonlocality in the plasmonic response of single triangular prisms and connected bowtie dimers. Our results demonstrate the complexity of the interplay between nonlocal and geometric effects taking place in these structures. We show the different sensitivities to both effects of the various plasmonic modes supported by these systems. Finally, we present an experimental electron-energy loss study on gold nanoprisms connected by bridges as narrow as 1.6 nm. The comparison with our theoretical predictions enables us to reveal in a phenomenological fashion the enhancement of absorption damping that occurs in these atomistic junctions due to quantum confinement and grain boundary electron scattering.

KEYWORDS: surface plasmons · electron-energy loss spectroscopy · spatial nonlocality · longitudinal plasmons · grain boundary electron scattering · quantum confinement

In recent years, innovations in the field of nanophotonics have led to a wealth of technological applications such as high-sensitivity chemical and biological sensing,[1] improved photovoltaic light harvesting,[2] signal processing based on active plasmonic nanostructures,[3] and electromagnetic (EM) field modulation using metamaterials.[4,5] All these devices have been possible as a result of the enormous progress that nanofabrication and optical characterization techniques have experienced lately. However, the increasing miniaturization of these components means that the EM modes they support begin to be influenced by regions of significant nonlocality, which arise when metals are structured at the nanoscale.[6] Currently, progress is being made toward a deeper understanding of the influence of nonlocality, or spatial dispersion, on the permittivity of metals using three complementary approaches: (1) phenomenological mesoscale models based on extensions of Maxwell's equations into the nonlocal regime using, for example, a hydrodynamic approach;[7−11] (2) time dependent many-body quantum treatments viable for small system sizes;[12,13] and (3) optical experiments probing extremely thin films[14,15]

* Address correspondence to
yangkwj@imre.a-star.edu.sg,
a.fernandez-dominguez@imperial.ac.uk.

Received for review May 8, 2013
and accepted June 19, 2013.

10.1021/nn402323t

and diminutive particles.[16,17] Out of these three, the hydrodynamic theory has advantages due to its ease of implementation, qualitative validity of results,[18,19] and the possibility to modulate the degree of nonlocality, offering theoretical insights into the way spatial dispersion modifies EM fields.[20]

From an experimental perspective, electron-energy loss spectroscopy[21,22] (EELS) offers a powerful technique that enables the nonperturbative near-field mapping of the photonic local density of states[23,24] with subnanometer spatial resolution.[25−27] This capability makes EELS an excellent candidate for the study of the nonlocal response of metallic nanostructures.[28−31] From the theoretical side, spatial dispersion in electron microscopy of simple metallic geometries has been thoroughly analyzed in the past.[32−35] However, the interpretation of EELS spectra from complex plasmonic devices has been limited for two reasons: First, even though general solutions of Maxwell's equations have been developed to describe the response of these systems driven by an electron beam,[26] their operation was restricted to the local limit. Second, in cases where full nonlocal EM solutions were used, the underlying models were limited to plane wave excitation,[29] with the implementation of an EELS excitation source in the nonlocal regime still lacking. Importantly, EELS sources offer access to the whole modal spectrum, whereas optical excitation only probes the so-called bright modes, which couple strongly with radiation. Thus, compared to focused illumination, the exploration of nonlocal effects through EELS promises more complete information about the interplay between nonlocality and geometry.

In this work, we develop for the first time a full three-dimensional hydrodynamic nonlocal solution of Maxwell's equations in the frequency domain[11] that implements the EELS source as a line current. This configuration mimics the experimental setup, and we show that the resultant equations can be readily solved using COMSOL Multiphysics, a commercial finite element solver. We then use our numerical approach to perform a comprehensive study of the emergence of nonlocal effects in connected gold nanoprisms, exploring all the relevant parameters of the system, and revealing the physical implications of spatial dispersion in this geometry. Finally, we use our theoretical model to gain insights into a set of EELS experimental results on lithographically defined gold bowties connected by bridges as narrow as 1.6 nm. This enables us to assess the impact of quantum effects in the EM properties of these plasmonic systems. Our experimental findings reveal that the effect of nonlocality on the EELS spectra for the nanoprisms connected by the narrowest (1.6 nm) bridge is masked by quantum confinement and grain boundary electron scattering effects. Our measurements indicate that these effectively increase the absorption damping experienced by the plasmon modes supported by the nanostructure.

THEORY

In an EELS experiment, electrons with a fixed kinetic energy in the 100 keV range are directed along a linear path passing close to a plasmonic target. These fast electrons excite localized surface plasmons, thereby transferring part of their kinetic energy to the target. The resulting loss in kinetic energy is measured with the EELS detector, which disperses the electrons by energy. Normalizing the total number of electrons recorded by the detector, an energy loss probability spectrum is obtained.

Our simulated EELS spectra are calculated following the approach outlined in ref 23, which yields the spectrally decomposed energy loss probability, $\Gamma_{\mathrm{EELS}}(\omega)$, for a fast electron moving at constant velocity v along a linear trajectory $\mathbf{r}_e(t)$. The moving electron results in a current density $\mathbf{j}(\mathbf{r},t) = -e\hat{\mathbf{v}}\delta[\mathbf{r} - \mathbf{r}_e(t)]$, where e is the electron charge. Assuming that this current is directed in the z-direction and performing a temporal Fourier transform, we obtain $\mathbf{j}(z,\omega) = -e\hat{\mathbf{z}}\delta[\mathbf{R} - \mathbf{R}_0]e^{i\omega z/v}$, where ω is the angular frequency and $\mathbf{R}_0 = (x_0,y_0)$ is the impact parameter of the electron trajectory.

The moving electron creates a background electric field, $\mathbf{E}_0(\mathbf{r},t)$, which in the presence of a metallic nanostructure results in an induced field, $\mathbf{E}^{\mathrm{ind}}(\mathbf{r},t)$. The energy lost by an electron moving along the path $\mathbf{r}_e(t)$ is then given by

$$W = e\int \mathrm{d}t\mathbf{v}\cdot\mathbf{E}^{\mathrm{ind}}[\mathbf{r}_e(t), t] \qquad (1)$$

The spectral decomposition of eq 1 can be obtained by writing the energy lost in terms of the energy loss probability as $W = \int \hbar\omega\Gamma_{\mathrm{EELS}}(\omega)\ \mathrm{d}\omega$. Expressing the induced electric field in frequency domain, and rewriting the time integral in eq 1 into a line integral over the electron path $z(t)$, we have

$$\Gamma_{\mathrm{EELS}}(\omega) = \frac{ve}{2\pi\hbar\omega}\int \mathrm{d}z Re[e^{-i\omega z/v}E_z^{\mathrm{ind}}(z,\omega)] \qquad (2)$$

where $E_z^{\mathrm{ind}}(z,\omega)$ is the z-component (parallel to the electron trajectory) of the induced electric field.

Equation 2 shows that the energy loss probability can be directly extracted from the induced electric field along the source current. In the following, we discuss briefly how $E_z^{\mathrm{ind}}(z,\omega)$ can be obtained from the frequency domain solution of Maxwell's equations within a nonlocal hydrodynamical model. In this frame, the total electric fields, $\mathbf{E}(\mathbf{r},\omega) = \mathbf{E}_0(\mathbf{r},\omega) + \mathbf{E}^{\mathrm{ind}}(\mathbf{r},\omega)$, within an arbitrary metallic nanostructure (the target in our EELS experiments) are described by the inhomogeneous wave equation

$$\nabla\times[\nabla\times\mathbf{E}(\mathbf{r},\omega)] = \frac{\omega^2}{c^2}\varepsilon_0\varepsilon_\infty\mathbf{E}(\mathbf{r},\omega) + i\mu_0\omega\mathbf{J}_{\mathrm{d}}(\mathbf{r},\omega) \qquad (3)$$

where the first and second source terms in the right-hand side account for the residual response of the positive ion cores and the nonlocal displacement current, respectively. Within the hydrodynamical Drude model, the transport equation for the nonlocal current $\mathbf{J}_\mathrm{d}(\mathbf{r},\omega)$ reads

$$\beta^2\nabla[\nabla\cdot\mathbf{J}_\mathrm{d}(\mathbf{r},\omega)]+\omega(\omega+i\gamma)\mathbf{J}_\mathrm{d}(\mathbf{r},\omega) = i\omega\omega_\mathrm{P}^2\varepsilon_0\varepsilon_\infty\mathbf{E}(\mathbf{r},\omega) \qquad (4)$$

Equation 4 governs the dynamics of the electron density within the metal nanostructure. The first term takes into account the electron–electron interactions within the hydrodynamic picture, and the remaining terms can be easily recognized as the usual Drude ones for a noninteracting electron gas. The nonlocal parameter β, which is a measure of the characteristic speed of a conduction electron, is equal, except for an adimensional factor, to the metal Fermi velocity.[6] Note that in the limit $\beta = 0$, eq 4 recovers the local approximation. All the calculations in this work are evaluated at $\beta = 0.0036c$, where c is the speed of light, which is a realistic value for gold.[17]

Contrary to the local picture, the simultaneous solution of eqs 3 and 4 yields the excitation of longitudinal plasmon modes within the metal bulk below the plasma frequency, ω_P.[36] The inclusion of this new field component in the metallic regions requires the introduction of an additional boundary condition, which in our case corresponds to the continuity of the normal component of the electric field.[37] It can be easily demonstrated that eqs 3 and 4 give the following longitudinal plasmon dispersion relation

$$k_\perp^2 = k_\parallel^2+\frac{1}{\beta^2}[\omega_\mathrm{P}^2-\omega(\omega+i\gamma)] \qquad (5)$$

where $k_\perp$ ($k_\parallel$) is the evanescent (propagating) wavevector along the direction normal (parallel) to the metal surface. In flat geometries and at frequencies much smaller than the plasma frequency, we can use the strongly evanescent nature of longitudinal plasmons to assume $k_\perp \gg k_\parallel$ and write $\delta_\mathrm{LP} = k_\perp^{-1} \approx \beta/\omega_\mathrm{P}$ for the longitudinal plasmons decay length. This result evidences the role of β as the parameter which controls the nonlocal thickening of the induced charge distribution at the metal boundaries.[20,38]

Finally, in order to obtain the induced electric fields required to evaluate eq 2, we follow a solving strategy similar to the one recently proposed to calculate the electric fields scattered by on-substrate nanoparticles under dark field illumination.[39,40] We first compute the vacuum electric fields produced by the EELS current in absence of the target, $\mathbf{E}_0(\mathbf{r},\omega)$. Subsequently, we inject these electric fields as the EM source in the simulation domain including the metal nanostructure. Thus, we can retrieve $\mathbf{E}^\mathrm{ind}(\mathbf{r},\omega) = \mathbf{E}(\mathbf{r},\omega) - \mathbf{E}_0(\mathbf{r},\omega)$ and compute $\Gamma_\mathrm{EELS}(\omega)$ from eq 2.

RESULTS AND DISCUSSION

We first apply our nonlocal EELS machinery to the study of single gold nanoprisms. Specifically, we consider nanoparticles with an equilateral triangular cross section of side L ranging from 5 to 200 nm, and height

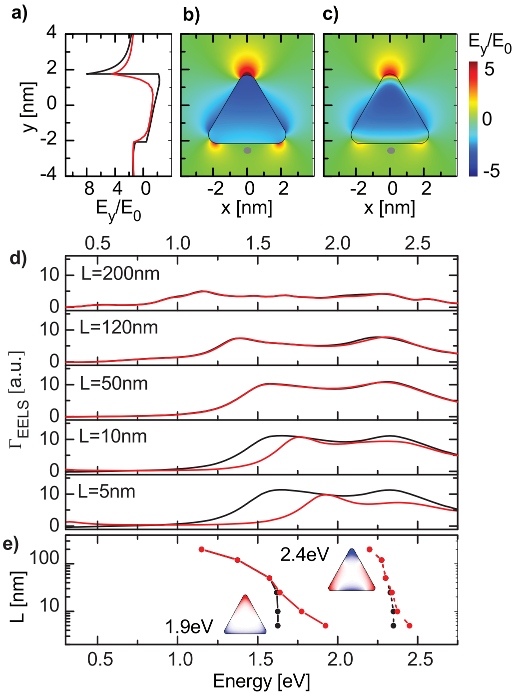

Figure 1. Simulated EELS response of single gold nanoprisms (height $D = 0.3L$) on a 0.5 nm chromium adhesion layer, supported by a SiN$_x$ membrane of thickness D. (a) Black and red lines plot local (1.6 eV) and nonlocal (1.9 eV) E_y^ind along the y-axis of a nanoprism with L = 5 nm. (b) Local E_y^ind map within the $z = D/2$ plane at 1.6 eV. (c) The same as panel b but under the nonlocal description and at 1.9 eV. In both panels, the saturated color scale ranges from positive (red) to negative (blue) electric field amplitude, and the position of the electron beam source is indicated by a gray dot. (d) Simulated local (black) and nonlocal (red) EELS spectra for single nanoprisms with various L. To make the system fully scalable, we have set the distance between target and source to 0.15L. (e) Trace of the spectral position of the modes identified in panel d. The insets show saturated nonlocal charge density maps (L = 5 nm) at the energies of the dipole (1.9 eV) and quadrupole (2.4 eV) modes.

$D = 0.3L$. The gold permittivity in our calculations corresponds to the Drude fitting to the experimental data in ref 41, as outlined in the Methods section at the end of this article. To mimic realistic experimental conditions, we place these plasmonic nanostructures on a SiN$_x$ supporting membrane with dielectric constant ε = 5. We also introduce a thin (~0.5 nm) chromium adhesion layer (with dielectric properties taken from ref 42) between target and membrane[43] (note that nonlocal effects in chromium have been neglected in our calculations due to the low value of the Fermi velocity ~β, which in chromium is 1 order of magnitude smaller than in gold[44]). Figure 1a–c plots the y-component of the electric field induced in an L = 5 nm triangle by an incident electron beam positioned 0.75 nm away from the center of one of its sides, as indicated by the gray dot in panels b and c. Panel a plots E_y^ind as a function of the y-coordinate along the nanoprism axis (x = 0, $z = D/2$). The electric fields are evaluated at the lowest plasmonic resonance supported by the nanostructure, and the black (red) line corresponds to local (nonlocal) predictions. Panels b and c render the local (1.6 eV) and nonlocal (1.9 eV) E_y^{ind}, respectively, within the $z = D/2$ plane. The plots of the y-component of the electric field (normal to one of the sides of the prisms) in Figure 1a−c illustrate the central manifestation of spatial dispersion, namely, the removal of the discontinuity of the normal component of the electric field at the metal boundaries. This smearing of the EM fields is concomitant with a decrease of the electric field amplitude. Note the 2-fold reduction in E_y^{ind} at the prism corner in panel a.

Figure 1d shows $\Gamma_{\mathrm{EELS}}(\omega)$ for gold nanoprisms with different L obtained within the local (black) and nonlocal (red) picture. To make the system fully scalable, we have set the distance between target and electron beam to $0.15L$. Note that the impact of spatial dispersion is more apparent in the spectral position of the EELS maxima than in its intensity. In panel e, the evolution of the resonant position for increasing prism side is rendered. The insets display saturated nonlocal charge density plots, $\rho \sim \nabla\cdot\mathbf{E}^{\mathrm{ind}}(\mathbf{r},\omega)$, evaluated at 1.9 and 2.4 eV for $L = 5$ nm. These plots enable us to classify the two resonances observed in the spectra as in-plane dipole and quadrupole plasmonic modes, respectively. Figure 1d allows us to bracket the point at which local and nonlocal predictions begin to diverge between $L = 10$ nm and $L = 50$ nm, which is in agreement with recent experimental findings on silver nanoparticles.[31,45] Interestingly, this onset of the nonlocal regime also corresponds to the nanoprism size range where local electrodynamics converges to the so-called quasi-static regime. In this limit, the energy of plasmonic modes is scale-invariant under the local approximation, making the spectral position of the EELS maxima independent of the overall size of the target. Figure 1e illustrates how the introduction of spatial dispersion in the metal permittivity gives rise to a continuous blue shifting of the plasmonic modes as L decreases. This effect can be linked to the continuous increasing of the relative size of the nonlocal surface charge thickening, given by the ratio δ_{LP}/L.

Interestingly, Figure 1 shows that the dipolar plasmon mode supported by gold nanoprisms is more sensitive to spatial nonlocality than its quadrupole counterpart. This can be qualitatively understood from the longitudinal plasmon dispersion given by eq 5. Note that, as the spectral position of both plasmonic modes is well below ω_{P}, the second term in the right-hand side of this equation acquires very similar values in both cases. However, the insets of Figure 1e evidence that the effective wavelength, which is inversely proportional to $k_{\|}$ and measures the spatial extent of the EM oscillations along the nanoparticle perimeter, is significantly shorter for the quadrupole mode. By estimating the effective wavelength of the plasmonic resonances through these charge plots, δ_{LP} can be calculated from eq 5. This yields a smaller longitudinal plasmon decay length for the higher order mode, which explains the lower impact that nonlocality has on its spectral position.

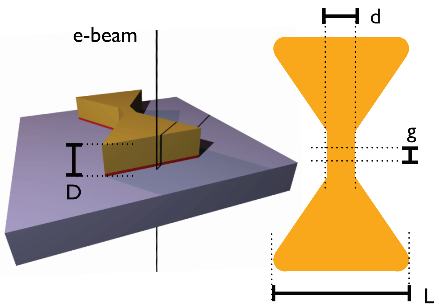

Figure 2. Geometry considered in our calculations. Two gold nanoprisms of height D and side length L, connected through a bridge of width d and length g (measured apex to apex). The resulting structure is separated from a SiN$_x$ supporting membrane through a 0.5 nm thick chromium adhesion layer. The impact parameter of the electron beam is $0.15L$ nm away from the center of the outer side of the connected nanoprisms.

Next, we perform a similar study for a structure consisting of a pair of gold nanoprisms of the same dimensions as the ones investigated in Figure 1. As illustrated in Figure 2, the two prisms are mirrored at their apex and connected through a gold bridge of variable shape. We choose this geometry instead of a separated configuration for two reasons. First, nonlocal effects in gapped nanoparticles have already been investigated lately.[38,46,47] Second, whereas relevant quantum tunnelling effects take place in angstrom-sized plasmonic gaps,[30,48] we can expect them to be negligible in conductive junctions, which makes connected geometries a more suitable platform for the analysis of spatial nonlocality. Figure 2 shows the various geometric parameters of the EELS target: prism side L, height D, and bridge width and length, d and g, respectively (note that the bridge length is measured from the points where the triangles apexes would have been in a disconnected dimer). We restrict our attention to electron beams impinging in the vicinity of the center of one of the outer sides of the nanoprisms. Again, in order to make the nanostructure scalable, we set the distance target-excitation to $0.15L$.

Figure 3 summarizes the findings of our EELS exploration of nonlocal effects in connected gold nanoprisms. Note that the lowest resonance supported by this geometry is a charge transfer plasmonic mode characterized by a large accumulation of positive and negative charges at opposite ends of the dimer. This mode cannot be described by plasmon hybridization,[49] as each of the resonant prisms, considered as isolated elements, does not satisfy charge neutrality. Figure 3a−c renders the electric field, E_y^{ind}, at the charge transfer mode, revealing that nonlocal effects diminish significantly the field localization that takes place around the connective bridge within the local

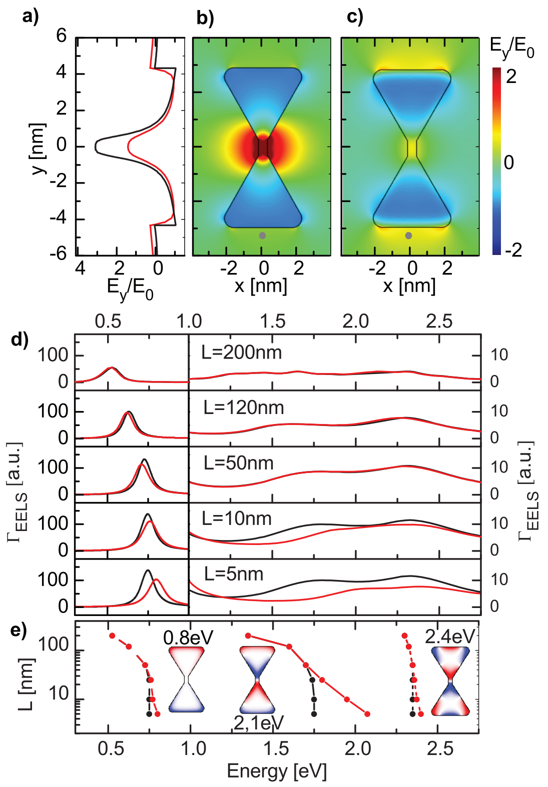

Figure 3. Simulated $\Gamma_{\mathrm{EELS}}(\omega)$ for connected gold nanoprisms of side length L and height $D = 0.3L$. The bridge width and length are $d = 0.1L$ and $g = 0$, respectively. The nanostructures are placed on top of a 0.5 nm chromium layer, and supported by a SiN_x membrane of thickness D. The distance target-excitation is $0.15L$. (a) Local (black) and nonlocal (red) E_y^{ind} along the y-axis for $L = 5$ nm evaluated at 0.75 and 0.8 eV, respectively. (b) Local E_y^{ind} maps within the $z = D/2$ plane at 0.75 eV. (c) The same as panel b but under the nonlocal description and at 0.8 eV. The position of the electron beam is indicated by a gray dot in both panels. (d) Simulated local (black) and nonlocal (red) $\Gamma_{\mathrm{EELS}}(\omega)$ for connected nanoprisms with L ranging from 5 to 200 nm. (e) Trace of the spectral position of the EELS maxima identified in panel d. The insets show saturated nonlocal charge density maps for the $L = 5$ nm dimer.

picture. The parameters of the structure are $L = 5$ nm, $D = 1.5$ nm, $d = 0.5$ nm, and $g = 0$ nm. Note that our theoretical model does not account for grain boundary and quantum confinement effects at the gold bridges, which are expected to strongly impact the electronic response of this system. We anticipate that these will be introduced in a phenomenological manner in our model at a later stage.

The field enhancement in this geometry is lower than in the single prism case (note that there is no lightning rod effect at the bowtie bridge). However, the relative impact of spatial dispersion is similar to the one observed in Figure 1, yielding as well a 2-fold reduction in E_y^{ind}. Panel a plots the local (black) and nonlocal (red) electric fields as a function of y ($x = 0$, $z = D/2$). Panels b and c display E_y^{ind} color maps at $z = D/2$ obtained under the local (0.75 eV) and nonlocal (0.8 eV) picture, respectively. These results show that the nonlocal smearing of the electric fields at the metal boundaries leads to a significant reduction of the field enhancement in the vicinity of the bowtie. This effect is particularly pronounced in the region of the narrow connective bridge, where the discrepancy between local and nonlocal predictions is largest.

Figure 3d plots $\Gamma_{\mathrm{EELS}}(\omega)$ obtained from nanoprism dimers with side length ranging from 5 to 200 nm. The nanostructure height is set to $D = 0.3L$, and the bridge geometric parameters are $d = 0.1L$ and $g = 0$. Local (nonlocal) results are shown in black (red) lines. Again, the effect of nonlocality is more pronounced in the resonance position than in their intensity. The EELS spectra for the bowties are dominated by the aforementioned charge transfer peak (note that Γ_{EELS} is ~10 times larger than all other resonances). To make the fingerprint of higher order plasmonic modes in the EELS signal apparent, the vertical axes below 1 eV have been rescaled. Three different EELS resonances can be identified in our theoretical spectra, in agreement with previous studies on similar gold nanostructures. Figure 3e renders their spectral position as a function of L. The insets show the charge distribution evaluated at the three EELS maxima for $L = 5$ nm. As anticipated, the low energy peak corresponds to the charge transfer mode. On the other hand, the two broader peaks at higher energies cannot be unambiguously characterized.[43] Both emerge in a frequency range where the structure supports two distinct but nearly degenerate plasmonic modes. Thus, the maximum between 1.4 and 2.1 eV (2.3 and 2.5 eV) originates from plasmonic modes corresponding to the parallel and antiparallel orientation of the dipole (quadrupole) resonances supported by single nanoprisms. In both cases, the charge configuration most efficiently excited by the incident electron beam is shown in the corresponding inset of Figure 3e ($L = 5$ nm).

Similarly to the case of isolated nanoprisms, the impact of spatial dispersion on connected bowties increases with smaller size. However, the phenomenology of the modes sensitivity is more complex than in the single-particle configuration. Figure 3e shows that both the charge transfer and the quadrupole–quadrupole peaks are rather robust to nonlocal effects. However, the dipole–dipole resonance presents a much higher sensitivity. Again, we can gain physical insight into these observations through eq 5. The rapid spatial oscillation of the quadrupole–quadrupole mode effectively enlarges the longitudinal plasmon parallel wavevector, and therefore the normal component as well. In a similar way, it is the frequency term in the dispersion relation which increases $k_\perp$ for the charge transfer mode. As a result, δ_{LP} is diminished in both cases. On the other hand, for the dipole–dipole EELS maximum, both the $k_\parallel$ and the frequency term in the right-hand side of eq 5 acquire intermediate values. Our results indicate that the balance between these two terms yields the longest δ_{LP}, in a similar way to the

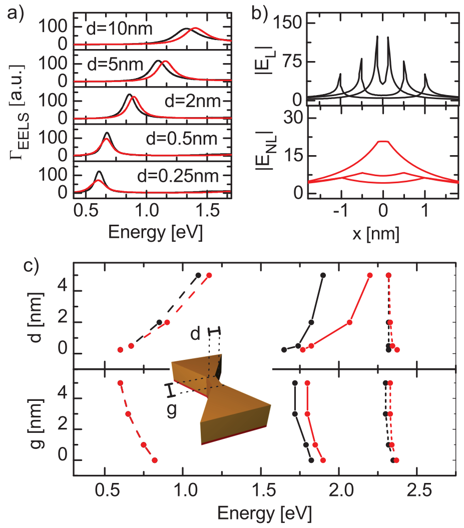

Figure 4. (a) Simulated local (black) and nonlocal (red) EELS spectra for gold nanoprisms connected by bridges of various widths, *d* (*L* = 10, *D* = 3, and *g* = 0 nm). The target configuration (substrate, adhesion layer, electric beam excitation) remain the same as in Figure 3. (b) Electric field amplitude along the bridge width for the three narrowest geometries in panel a. Top (bottom) profiles correspond to local (nonlocal) calculations. (c) Trace of the local (black) and nonlocal (red) resonances for connected nanoprisms against *d* (top, *g* = 0 nm) and against *g* (bottom, *d* = 1 nm).

dipole mode supported by a single nanoprism. Note that the nonlocal blueshift experienced by the lower energy resonance in Figure 1 resembles the one observed in Figure 3 for this mode.

The spectral properties of the plasmon modes supported by gold bowties are highly sensitive not only to the dimensions of the connected nanoprisms (as we have demonstrated above), but also to the geometry of the junction between them. This makes these structures very attractive candidates for photonic applications that rely on the precise engineering of one or several EM resonances over a wide frequency window.[50−52] In the following, we investigate how the high tunability featured by these plasmonic devices within the local approximation is affected by spatial dispersion. In Figure 4a, the effect of the bridge width on the charge transfer mode is analyzed for connected nanoprisms with *L* = 10 nm and *D* = 3 nm. Local (black) and nonlocal (red) EELS spectra for *d* ranging from 0.25 to 10 nm are plotted (*g* = 0 nm). Interestingly, our results show that the impact of spatial dispersion on the position of the EELS maxima is higher at larger *d*. This is a surprising result, as it seems to contradict our previous observations which showed the enhancement of nonlocal effects with decreasing nanoparticle size, *L*. However, note that the thickest bridge (*d* = 10 nm) yields a rectangular-shaped nanoparticle, and the EELS peak in this case originates from a dipole mode similar to the one we identified in Figure 1 for single prisms. On the other hand, *d* = 0.25 nm corresponds to a connected dimer like the ones in Figure 3, and we can link the maximum in $\Gamma_{EELS}(\omega)$ to a charge transfer plasmonic mode. As we showed above, the former is very sensitive to nonlocality, whereas the latter is much more robust. This explains the spectral trends that we observe in Figure 4a.

To gain further physical insight into the interplay between geometric and nonlocal effects at the dimer bridge, we plot in panel b of Figure 4 the local (top) and nonlocal (bottom) electric field amplitude across (*x*-direction) the bridge for the three narrowest bowties in panel a. These profiles are evaluated at resonance and indicate that the electric field is significantly amplified at the junction for small *d*, whereas it remains moderate for wider geometries. In narrow bridges, the nonlocal smearing of the electron density effectively pushes the plasmonic modes into the metal regions, while decreasing their parallel wavevector. These manifestations of spatial nonlocality lead to the slower variation of the electric field amplitudes across the nanoprism junctions in panel b. Note that, although the field accumulation for the narrow bridges does not lead to an apparent nonlocal shift of the EELS maxima, it gives rise to the highest reduction in their intensity in panel (a). In the top panel of Figure 4c, the spectral position of the EELS resonances is plotted against *d* for bridges narrower than 4 nm (*g* = 0 nm). In this panel, the three resonances supported by the nanostructure are investigated. As we already observed in Figure 3, the dipole−dipole peak at intermediate energies is the most affected by nonlocality, which also increases its sensitivity to the bridge width. In the bottom panel of Figure 4c, the effect of the bridge length *g* is investigated (*d* = 1 nm). This panel indicates that the bowtie resonances investigated here, even within the nonlocal description, can be only slightly tuned through this geometric parameter.

Current experimental capabilities make the accurate fabrication and characterization of plasmonic EELS samples shaped at the nanometer scale possible. Here, we present EELS measurements performed on a single gold bowtie antenna of 70 nm side length and 20 nm height. This target was fabricated onto a 30-nm-thick SiN_x membrane using methods previously described[27,43,53] (see the Methods section for further details). Shifts in the charge transfer plasmon mode were due only to variations in the bridge geometry, and not variations from one bowtie to another. This controlled experiment was achieved by performing local electron-beam sculpting (ablation) of the bridge region (to be detailed separately). Doing so allowed EELS spectra obtained from bridges of different widths (but of identical prisms) to be consistently compared with each other, as plotted in Figure 5a. As the bridge width was decreased from *d* = 7 nm to *d* = 1.6 nm, the charge transfer plasmon peak red-shifted slightly but decreased significantly in intensity. Remarkably, these experimental results show that charge-transfer plasmons

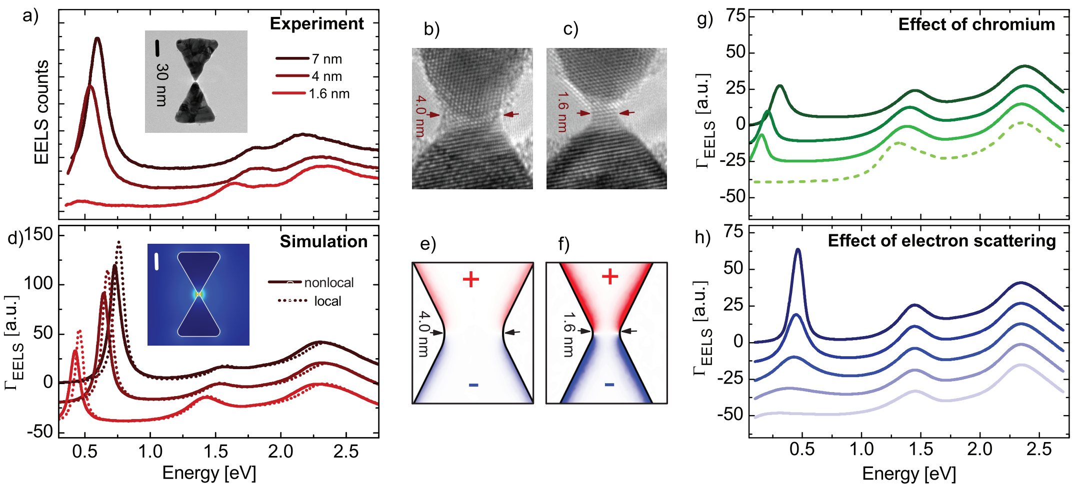

Figure 5. **(a) Experimental EELS spectra for connected gold nanoprisms with $L = 70$ nm, $D = 20$ nm, and $d = 1.6$ nm, 4 and 7 nm. The bowties are placed on top of a 1 nm chromium layer and are supported by a 30 nm thick SiN_x membrane. The inset shows a transmission electron microscopy (TEM) image of one of the samples. (b and c) TEM images zooming at the two narrowest connective bridges. (d) Local (dotted lines) and nonlocal (solid lines) simulations mirroring the experimental geometries in panel a. (e and f) Nonlocal charge density maps evaluated at the charge transfer resonance for the geometries modeling the bridges in panels b and c. (g) Local $\Gamma_{EELS}(\omega)$ for bowties with $d = 1.6$ nm and chromium bridges of height 5, 2, 1, and 0 nm (from top to bottom). (h) The same as panel g but for 1 nm chromium thickness and increasing Drude damping frequency at the gold bridge, effectively modeling grain boundary electron scattering effects. The top (bottom) spectrum corresponds to an increase in the gold damping frequency by a factor of 1 (75) with respect to the prism regions.**

can still be supported across a bridge that is only 6 atoms across, as seen in Figure 5c.

We investigate the emergence of nonlocal effects in samples with bridge widths as small as 1.6 nm both theoretically and experimentally. In Figure 5a, the EELS spectra measured from three of these nanostructures (see inset for a TEM image) are plotted. Panels b and c display TEM images of the two narrowest junctions, d = 4 and 1.6 nm. Importantly, our experimental spectra show the signature of the plasmonic modes predicted theoretically for the structure. In agreement with the numerical $\Gamma_{EELS}(\omega)$ in Figure 3, the lowest energy EELS maxima stand out in the measured EELS profiles. Note that the height of this peak diminishes drastically in the 1.6 nm bridge case. As expected from the numerical trends in Figure 4c, the charge transfer and the dipole–dipole resonances are more sensitive to the bridge geometry and red-shift significantly with decreasing d. On the other hand, the quadrupole–quadrupole mode (the highest in energy) emerges at roughly the same position for the three samples.

Figure 5d show numerical $\Gamma_{EELS}(\omega)$ mimicking the experimental conditions. The model geometries in the calculations are set in accordance to the nominal dimensions of the measured samples. Dashed and solid lines correspond to local and nonlocal calculations, respectively. We can observe the good agreement with the spectra in panel a, in particular for the two widest bridges. Our theoretical results also show the low impact that nonlocality has on the connected geometries explored in the experiments. Note that the main nonlocal feature in the EELS spectra is the further red-shift of the charge transfer mode with decreasing d. This red-shift is a striking result, because it is contrary to the phenomenology observed in single nanoparticles[31] and gapped dimers,[17] where spatial dispersion always increases the surface plasmon resonant energies. Note that a slight (0.01 eV) nonlocal red-shift of the EELS maximum (with respect to the local prediction) can be also observed in the bottom spectrum of Figure 4a. We can understand this spectral lowering of the charge transfer mode as a consequence of the effective narrowing of the bridge width associated to the nonlocal smearing of the surface charge distribution at the metal boundaries.[54,55] This interpretation is supported by the nonlocal charge density maps at the bridge areas displayed in Figure 5e,f. These are evaluated at the charge transfer resonance for the two narrowest bridges. Note that the color scale is the same for both structures, demonstrating the effective narrowing of the connective bridge associated to the nonlocal thickening of the surface charge distribution in the d = 1.6 nm case.

Our theoretical EELS spectrum does not reproduce the drastic reduction of the charge transfer peak found in the experiments for the 1.6 nm thick bridge. This means that spatial dispersion is not the cause for the severe lowering in the experimental EELS signal, and that the physical mechanism inhibiting the charge transfer plasmonic mode is not reflected in our theoretical description. To explain the drastic reduction in peak height as the bridge was narrowed, we turn to three plausible considerations, all of which result in drastically reduced conductance by the bridge. First, we consider the case in which the gold bridge has been removed and only chromium atoms remained at the junction. We realize that this is an unlikely case because the gold lattice fringes can be seen in the TEM image to extend from the individual nanoprisms into the bridge region. Nevertheless, Figure 5g plots $\Gamma_{\mathrm{EELS}}(\omega)$ for nanoprisms with chromium bridges ranging from 5 nm (top) to 0 nm (bottom). Note that the bottom spectrum (dashed line) corresponds to a separated bowtie, which does not exhibit the charge transfer EELS maximum. We can observe that the reduction of the chromium bridge leads to a continuous red-shift of the lower energy EELS resonance similar to the one associated to the decrease in d in Figure 4c. This allows us to discard this consideration, as it does not reproduce the drastic reduction in peak height observed experimentally, and overestimates the red-shift of the peaks as the bridge was narrowed.

A second possibility is that quantum confinement present in the bridge has lowered the conductance substantially by offering a reduced number of open channels. The increased effective resistivity can be included by an enhanced Drude damping in the bridge.[56] The third plausible origin of the drastic decrease in $\Gamma_{\mathrm{EELS}}(\omega)$ at the charge transfer mode for narrow bridges is as follows, and can be described also by an increased Drude damping. The TEM images in Figure 5b,c show the polycrystalline character of the bridges connecting the nanoprisms. Upon careful inspection, it is evident that the crystal orientations in the nanoprisms are different, and merge at a single grain boundary that spans the entire cross section of the $d = 1.6$ nm bowties. Grain boundaries have been described as tunnel-barriers for electron transport that introduce electron surface scattering[57] and therefore increase the Drude damping rate. Note that this effect is inversely proportional to the metallic cross sectional area, and therefore, we can expect that this damping mechanism will be larger for narrower bridges. To capture the effect of this locally enhanced resistance, we increased the gold Drude damping only at the junction of $d = 1.6$ nm bowties. This phenomenological treatment of electron scattering is inspired in the so-called *quantum corrected model*, in which the effect of quantum tunnelling at the subnanometric gap between two metallic nanoparticles is modeled through an effective Drude permittivity with high absorption losses.[13] Figure 5h plots the EELS spectra obtained by increasing the damping frequency in our local calculations by a factor of 1, 10, 25, 50, and 75 (top to bottom) with respect to the gold prism regions. These numbers are in good agreement with the resistivity enhancement due to electron scattering reported for polycrystalline gold nanowires with grain sizes ranging from a few nanometers to a few angstroms.[58] Our results indicate that this increase in Drude damping yields the observed reduction in the charge transfer peak, without altering its spectral position. Note as well that the higher energy plasmonic modes are not affected significantly by the increase in absorption losses at the prisms junction. Therefore, we can conclude that either quantum confinement or grain boundary electron scattering, or a combination of the two, is likely to be the cause of the disagreement between our theoretical and experimental results for 1.6 nm thick bridges.

CONCLUSION

In summary, we have developed a three-dimensional nonlocal hydrodynamic solution of Maxwell's equations in order to investigate the electron-energy loss probing of nonlocal effects in metals structured below the nanoscale. Applying our theoretical model to single gold prisms, we have bracketed the onset of the regime of significant nonlocality for this geometry between 10 and 50 nm prism side length. We have extended our study to connected bowties, where the phenomenology associated to spatial dispersion is richer, analyzing the interplay between nonlocal and geometric effects for this structure in detail. Using the longitudinal plasmon decay length as a key magnitude, we have shed light into the different degrees of nonlocal sensitivity exhibited by the various plasmonic modes supported by these two nanoparticle configurations. For connected bowties, we show that it is the dipole–dipole mode that is most affected by nonlocality, resulting in blueshifts as large as 0.7 eV for a dimer made up of prisms with side length of 5 nm. Finally, we have presented experimental electron-energy loss spectra for gold nanoprisms connected by bridges as narrow as 1.6 nm. Here, nonlocal effects do not appear to be pronounced. Our results reveal that, in contrast to nonlocal models which treat metals as completely homogeneous, quantum confinement and granularity at the nanometer scale need to be taken into consideration. In particular, comparison with our theoretical predictions has enabled us to reveal the strong additional damping that occurs in plasmonic nanostructures connected by diminutive junctions.

METHODS

Finite Element Simulations. As outlined in the Theory section, the EELS source was implemented as a line current of the form $\mathbf{j}(z,\omega) = -e\hat{\mathbf{z}}\delta[\mathbf{R} - \mathbf{R}_0]e^{i\omega z/v}$ in COMSOL Multiphysics, a commercial differential equations solver implementing the finite element method (note that ω is the angular frequency and $\mathbf{R}_0 = (x_0,y_0)$ is the impact parameter of the electron trajectory). Next, the Maxwell's wave equation (eq 3) and the hydrodynamic transport equation (eq 4) were solved simultaneously using the multifrontal massively parallel sparse direct solver (MUMPS).[59]

Highly nonuniform tetrahedral discretization meshes were used to resolve accurately the different length scales involved in the solution of the coupled set of equations. The finest details of the nanostructures were mapped manually using grid spacings as narrow as 0.01 nm. The electron beam, the substrate and the metallic nanostructures were enclosed by a spherically symmetric perfectly matched layer (PML) that efficiently absorbs scattered EM waves. The convergence of the calculations against simulation volume, EELS line current source length, mesh resolution and PML thickness was checked systematically for variations in each of these parameters.

The gold permittivity in our calculations corresponds to the Drude fitting to the experimental data in ref 41, with a Drude plasma frequency parameter $\omega_P = 4.6$ eV, damping parameter $\gamma = 0.071$ eV, and background permittivity $\varepsilon_\infty = 3.46$. The dielectric properties for the chromium adhesion layer were taken from ref 42.

For each frequency point, we performed two simulations based on an identical mesh: first, the background electric field, $\mathbf{E}_0(\mathbf{r},\omega)$, is determined in the absence of the metallic nanostructure. Then, the metallic structure is added and the full field $\mathbf{E}(\mathbf{r},\omega)$ is calculated. Once these quantities are known, the induced field is straightforwardly evaluated by $\mathbf{E}^{\text{ind}}(\mathbf{r},\omega) = \mathbf{E}(\mathbf{r},\omega) - \mathbf{E}_0(\mathbf{r},\omega)$.

Sample Fabrication. Gold nanoprism pairs with bridge size of ~6 nm were first fabricated onto 30-nm-thick silicon nitride (SiN_x) membranes using electron-beam lithography combined with a lift-off process. The prisms consisted of 20 nm thick Au on an ~1 nm Cr adhesion layer, evaporated by an electron-beam evaporator. To further shrink the bridge size of the connected nanoprism pairs, they were loaded into a high-resolution transmission electron microscope (FEI Titan) for focused-electron-beam nanosculpting. In brief, we used a focused, 200 keV electron beam in STEM mode to irradiate the bridge junction region to remove the atoms slowly. Every minute or so, a STEM image was taken to monitor the evolution of the bridge and correct for specimen drift. Depending on the beam current, beam size, and the nanosculpting time, we were able to control the bridge size with atomic precision. The smallest bridge size was limited by surface diffusion of the gold atoms during imaging and by the stress in the bridge that was introduced when the specimen was taken in-and-out of the TEM between sessions in this multisession experiment.

EELS Characterization. In between each sculpting session, EELS was performed in STEM mode on the same FEI Titan TEM with Schottky electron source, now operated at 80 kV. The electron beam was focused to a probe with a diameter less than 1 nm, using a convergence semiangle of 13 mrad. Attached to the TEM was a Gatan Tridiem ER EELS detector for EELS mapping and spectroscopy, for which a 6 mrad collection semiangle was applied. A Wien-type monochromator dispersed the electron beam in energy, and a narrow energy-selecting slit formed a monochrome electron beam with typical full-width at half-maximum values of 60−70 meV and full width at 1/1000 of maximum values of 0.7 eV. EELS was acquired with a modified binned gain averaging routine. In brief, individual spectra were acquired fast, with illumination periods around 40 ms, using 16 times on-chip binning for detector CCD readout. No gain or dark signal was corrected during acquisition; the detector channel-to-channel gain variation was averaged out by constantly changing the readout location and correcting for these shifts after completing the EELS acquisition. A high-quality dark reference was acquired separately, and used for postacquisition dark signal correction. Spectra shown are typically summations of 1000 individual, aligned spectra. The spectra were normalized by giving the maximum of the spectra (the top of the zero-loss peak) the same value. All spectra were acquired 1−2 nm away from the metal surfaces, axially at the long edge of the nanoprism pair. The background signal was subtracted by fitting a high-quality, premeasured spectrum from only the SiN_x membranes, far away from any deposited gold.

Conflict of Interest: The authors declare no competing financial interest.

Acknowledgment. This work was supported by the EPSRC Active Plasmonics Programme, the Centre for Doctoral Training on Theory and Simulation of Materials (TSM-CDT), the ESF Plasmon-Bionanosense Network, and the Leverhulme Trust. J.K.W.Y. and M.B. kindly acknowledge support from The Singapore National Research Foundation (NRF) under the CRP program (Award Nos. NRF-2011, NRF-CRP 001-126 and NRF-CRP 8-2011-07). H.D. thanks the sponsorship from National Science Foundation of China (Grant Nos. 11274107 and 61204109). A.I.F.-D. and J.B.P. would like to acknowledge the funding provided by the Gordon and Betty Moore Foundation. This work made use of the high-resolution electron-beam lithography and monochromated electron-energy loss spectroscopy facilities IMRE.

REFERENCES AND NOTES

1. Xu, H.; Bjerneld, E.; Käll, M.; Börjesson, L. Spectroscopy of Single Hemoglobin Molecules by Surface Enhanced Raman Scattering. *Phys. Rev. Lett.* **1999**, *83*, 4357–4360.
2. Atwater, H. A.; Polman, A. Plasmonics for Improved Photovoltaic Devices. *Nat. Mater.* **2010**, *9*, 205–213.
3. Krasavin, A. V.; Zheludev, N. I. Active Plasmonics: Controlling Signals in Au/Ga Waveguide Using Nanoscale Structural Transformations. *Appl. Phys. Lett.* **2004**, *84*, 1416–1418.
4. Smith, D. R.; Pendry, J. B.; Wiltshire, M. C. K. Metamaterials and Negative Refractive Index. *Science* **2004**, *305*, 788.
5. Schurig, D.; Mock, J. J.; Justice, B. J.; Cummer, S. A.; Pendry, J. B.; Starr, A. F.; Smith, D. R. Metamaterial Electromagnetic Cloak at Microwave Frequencies. *Science* **2006**, *314*, 977.
6. Boardman, A. D. *Electromagnetic Surface Modes*; Wiley: New York, 1982.
7. Fuchs, R.; Claro, F. Multipolar Response of Small Metallic Spheres: Nonlocal Theory. *Phys. Rev. B* **1987**, *35*, 3722–3727.
8. Ruppin, R. Extinction Properties of Thin Metallic Nanowires. *Opt. Commun.* **2001**, *190*, 205–209.
9. García de Abajo, F. J. Nonlocal Effects in the Plasmons of Strongly Interacting Nanoparticles, Dimers, and Waveguides. *J. Phys. Chem. C* **2008**, *112*, 17983–17987.
10. Raza, S.; Toscano, G.; Jauho, A.-P.; Wubs, M.; Mortensen, N. A. Unusual Resonances in Nanoplasmonic Structures Due to Nonlocal Response. *Phys. Rev. B* **2011**, *84*, No. 121412(R).
11. Wiener, A.; Fernández-Domnguez, A. I.; Horsfield, A. P.; Pendry, J. B.; Maier, S. A. Nonlocal Effects in the Nanofocusing Performance of Plasmonic Tips. *Nano Lett.* **2012**, *12*, 3308–3314.
12. Zuloaga, J.; Prodan, E.; Nordlander, P. Quantum Description of the Plasmon Resonances of a Nanoparticle Dimer. *Nano Lett.* **2009**, *9*, 887–891.
13. Esteban, R.; Borisov, A. G.; Nordlander, P.; Aizpurua, J. Bridging Quantum and Classical Plasmonics with a Quantum-Corrected Model. *Nat. Commun.* **2012**, *3*, 825.
14. Anderegg, M.; Feuerbacher, B.; Fitton, B. Optically Excited Longitudinal Plasmons in Potassium. *Phys. Rev. Lett.* **1971**, *27*, 1565–1568.
15. Lindau, I.; Nilsson, P. Experimental Verification of Optically Excited Longitudinal Plasmons. *Phys. Scr.* **1971**, *3*, 87.
16. Palomba, S.; Novotny, L.; Palmer, R. E. Blue-Shifted Plasmon Resonance of Individual Size-Selected Gold Nanoparticles. *Opt. Commun.* **2008**, *281*, 480–483.
17. Ciraci, C.; Hill, R. T.; Mock, J. J.; Urzhumov, Y.; Fernandez-Dominguez, A. I.; Maier, S. A.; Pendry, J. B.; Chilkoti, A.; Smith, D. R. Probing the Ultimate Limits of Plasmonic Enhancement. *Science* **2012**, *337*, 1072–1074.
18. Stella, L.; Zhang, P.; García-Vidal, F. J.; Rubio, A.; García-González, P. Performance of Nonlocal Optics when Applied to Plasmonic Nanostructures. *J. Phys. Chem. C* **2013**, *117*, 8941–8949.
19. Teperik, T. V.; Nordlander, P.; Aizpurua, J.; Borisov, A. G. Robust Subnanometric Plasmon Ruler by Rescaling of the Nonlocal Optical Response. *Phys. Rev. Lett.* **2013** in press.
20. Fernández-Domnguez, A. I.; Wiener, A.; García-Vidal, F. J.; Maier, S. A.; Pendry, J. B. Transformation-Optics Description of Nonlocal Effects in Plasmonic Nanostructures. *Phys. Rev. Lett.* **2012**, *108*, 106802.
21. Echenique, P. M.; Rivacoba, A.; Zabala, N.; Ritchie, R. H. Electron Energy Loss in STEM Spectra. *Springer Proc. Phys.* **1991**, *62*, 127–134.
22. Egerton, R. F. Electron Energy-Loss Spectroscopy in the TEM. *Rep. Prog. Phys.* **2009**, *72*, 016502.

23. García de Abajo, F.; Kociak, M. Probing the Photonic Local Density of States with Electron Energy Loss Spectroscopy. *Phys. Rev. Lett.* **2008**, *100*, 106804.
24. Hohenester, U.; Ditlbacher, H.; Krenn, J. Electron-Energy-Loss Spectra of Plasmonic Nanoparticles. *Phys. Rev. Lett.* **2009**, *103*, 106801.
25. Bosman, M.; Keast, V. J.; Watanabe, M.; Maaroof, A. I.; Cortie, M. B. Mapping Surface Plasmons at the Nanometre Scale with an Electron Beam. *Nanotechnology* **2007**, *18*, 165505.
26. Nelayah, J.; Kociak, M.; Stéphan, O.; García de Abajo, F. J.; Tencé, M.; Henrard, L.; Taverna, D.; Pastoriza-Santos, I.; Liz-Marzán, L. M.; Colliex, C. Mapping surface plasmons on a single metallic nanoparticle. *Nat. Phys.* **2007**, *3*, 348–353.
27. Koh, A. L.; Fernández-Domnguez, A. I.; McComb, D. W.; Maier, S. A.; Yang, J. K. W. High-Resolution Mapping of Electron-Beam-Excited Plasmon Modes in Lithographically Defined Gold Nanostructures. *Nano Lett.* **2011**, *11*, 1323–1330.
28. Ouyang, F.; Batson, P. E.; Isaacson, M. Quantum Size Effects in the Surface-Plasmon Excitation of Small Metallic Particles by Electron-Energy-Loss Spectroscopy. *Phys. Rev. B* **1992**, *46*, 15421–15425.
29. Raza, S.; Stenger, N.; Kadkhodazadeh, S.; Fischer, S. V.; Kostesha, N.; Jauho, A.-P.; Burrows, A.; Wubs, M.; Mortensen, N. A. Blueshift of the Surface Plasmon Resonance in Silver Nanoparticles Studied with EELS. *Nanophotonics* **2013**, *2*, 131.
30. Scholl, J.; Garcia-Etxarri, A.; Koh, A.; Dionne, J. Observation of Quantum Tunneling Between two Plasmonic Nanoparticles. *Nano Lett.* **2013**, *13*, 564.
31. Scholl, J. A.; Koh, A. L.; Dionne, J. A. Quantum Plasmon Resonances of Individual Metallic Nanoparticles. *Nature* **2012**, *483*, 421–427.
32. Echenique, P. M.; Ritchie, R. H.; Barberán, N.; Inkson, J. Semiclassical Image Potential at a Solid Surface. *Ultramicroscopy* **1981**, *23*, 6486–6493.
33. Zabala, N.; Echenique, P. M. Energy Loss of Fast Electrons Moving Near Plane Boundaries with Dispersive Media. *Ultramicroscopy* **1990**, *32*, 327.
34. Pitarke, J.; Silkin, V.; Chulkov, E.; Echenique, P. Theory of Surface Plasmons and Surface-Plasmon Polaritons. *Rep. Prog. Phys.* **2007**, *70*, 1.
35. Rivacoba, A.; Zabala, N.; Aizpurua, J. Image Potential in Scanning Transmission Electron Microscopy. *Prog. Surf. Sci.* **2000**, *65*, 1.
36. Ciraci, C.; Pendry, J. B.; Smith, D. R. Hydrodynamic Model for Plasmonics: a Macroscopic Approach to a Microscopic Problem. *ChemPhysChem* **2013**, *14*, 1109–1116.
37. Moreau, A.; Ciraci, C.; Smith, D. R. Impact of Nonlocal Response on Metallodielectric Multilayers and Optical Patch Antennas. *Phys. Rev. B* **2013**, *87*, 045401.
38. Fernández-Domímguez, A. I.; Zhang, P.; Maier, S. A.; García-Vidal, F. J.; Pendry, J. B. Transformation-Optics Insight into Nonlocal Effects in Separated Nanowires. *Phys. Rev. B* **2012**, *86*, 241110R.
39. Moreau, A.; Ciraci, C.; Smith, D. R. Influence of Excitation and Collection Geometry on the Dark Field Spectra of Individual Plasmonic Nanostructures. *Opt. Express* **2010**, *18*, 2579–2587.
40. Lei, D.-Y.; Fernández-Domínguez, A. I.; Sonnefraud, Y.; Kannatassen, A.; Haglund, R. F. J.; Pendry, J. B.; Maier, S. A. Revealing Plasmonic Gap Modes in Particle-on-Film Systems Using Dark-Field Spectroscopy. *ACS Nano* **2012**, *6*, 1380–1386.
41. Palik, E. D. *Handbook of Optical Constants of Solids*; Handbook Series; Academic Press: New York, 1985.
42. Rodrigo, S.; García-Vidal, F.; Martin-Moreno, L. Influence of Material Properties on Extraordinary Optical Transmission Through Hole Arrays. *Phys. Rev. B* **2008**, *77*, 075401.
43. Duan, H.; Fernández-Domnguez, A. I.; Bosman, M.; Maier, S. A.; Yang, J. K. W. Nanoplasmonics: Classical down to the Nanometer Scale. *Nano Lett.* **2012**, *12*, 1683–1689.
44. Tsunoda, Y.; Hamaguchi, Y.; Kunitomi, N. Neutron Scattering Measurements in Chromium near the Neel Temperature. *J. Phys. Soc. Jpn.* **1972**, *32*, 394–399.
45. Haberland, H. Looking from Both Sides. *Nature* **2013**, *494*, E1–E2.
46. Toscano, G.; Raza, S.; Jauho, A.-P.; Mortensen, N. A.; Wubs, M. Modified Field Enhancement in Plasmonic Nanowire Dimers Due to Nonlocal Response. *Opt. Express* **2012**, *20*, 4146.
47. David, C.; García de Abajo, F. J. Spatial Nonlocality in the Optical Response of Metal Nanoparticles. *J. Phys. Chem. C* **2011**, *115*
48. Savage, K. J.; Hawkeye, M. M.; Esteban, R.; Borisov, A. G.; Aizpurua, J.; Baumberg, J. J. Revealing the Quantum Regime in Tunnelling Plasmonics. *Nature* **2012**, *491*, 574–577.
49. Prodan, E.; Radloff, C.; Halas, N. J.; Nordlander, P. A Hybridization Model for the Plasmon Response of Complex Nanostructures. *Science* **2003**, *302*, 5644.
50. Anker, J. N.; Hall, W. P.; Lyandres, O.; Shah, N. C.; Zhao, J.; Van Duyne, R. P. Biosensing with Plasmonic Nanosensors. *Nat. Mater.* **2008**, *7*, 442–453.
51. Bharadwaj, P.; Deutsch, B.; Novotny, L. Optical Antennas. *Adv. Opt. Photonics* **2009**, *1*, 438–483.
52. Giannini, V.; Fernández-Domínguez, A. I.; Sonnefraud, Y.; Roschuk, T.; Fernández-García, R.; Maier, S. A. Controlling Light Localization and Light-Matter Interactions with Nanoplasmonics. *Small* **2010**, *6*, 2498–2507.
53. Koh, A. L.; McComb, D. W.; Maier, S. A.; Low, H. Y.; Yang, J. Sub-10 nm Patterning of Gold Nanostructures on Silicon-Nitride Membranes for Plasmon Mapping with Electron Energy-Loss Spectroscopy. *J. Vac. Sci. Technol., B* **2010**, *28*, C6O45.
54. Fernández-Domínguez, A. I.; Luo, Y.; Wiener, A.; Pendry, J. B.; Maier, S. A. Theory of Three-Dimensional Nanocrescent Light Harvesters. *Nano Lett.* **2012**, *12*, 5946–5953.
55. Luo, Y.; Fernández-Domínguez, A. I.; Wiener, A.; Maier, S. A.; Pendry, J. B. Local Analogue to Spatial Nonlocality **2013**, submitted for publication.
56. Pérez-González, O.; Zabala, N.; Borisov, A. G.; Halas, N. J.; Nordlander, P.; Aizpurua, J. Optical Spectroscopy of Conductive Junctions in Plasmonic Cavities. *Nano Lett.* **2010**, *10*, 3090–3095.
57. Bietsch, A.; Michel, B. Size and Grain-Boundary Effects of a Gold Nanowire Measured by Conducting Atomic Force Microscopy. *Appl. Phys. Lett.* **2002**, *80*, 3346.
58. Zhu, L.; Jin, K.; Zheng, X. Effect of Quantum Transport on the Resistivity of Metal Nanocrystalline Materials in an Electric Field. *Appl. Phys. Lett.* **2007**, *91*, 103108.
59. Amestoy, P. R.; Duff, I. S.; L'Excellent, J. Y. Multifrontal Parallel Distributed Symmetric and Unsymmetric Solvers. *Comput. Methods Appl. Mech. Eng.* **2000**, *184*, 501–520.